Towards a complete Himalayan hydrologic budget: The spatiotemporal distribution of snowmelt and rainfall and their impact on river discharge

Bodo Bookhagen[1], Douglas W. Burbank[2]

1Geography Department, UC Santa Barbara, Santa Barbara, CA 93106, USA

2Institute for Crustal Studies, UC Santa Barbara, Santa Barbara, CA 93106, USA

Supplementary data

Data processing

1. Topographic data

Because the SRTM data are not continuous, we filled minor holes of a few pixels by interpolation and filled larger holes with 90-m elevation-adjusted Digital Terrain Elevation Data (DTED). For the remaining regions with missing topographic information, we used digital elevation models (DEMs) created from stereo-views of the Advanced Spaceborne Thermal Emission and Reflection Radiometer (ASTER).

2. Rainfall data

We used raw, orbital satellite data from the Tropical Rainfall Measurement Mission (TRMM) to estimate rainfall amounts [*Kummerow et al.*, 1998; *Kummerow et al.*, 2000]. The TRMM product 2B31provides rainfall estimates on a 4 x 6 km^2 pixel size between 36°N and 36°S. During processing, we interpolated every orbit onto an equally-spaced 5 x 5 km^2 grid. [Product 2B31, algorithm V6, more information are available at: http://disc.sci.gsfc.nasa.gov/precipitation/documentation/TRMM_README/TRMM_2B31_readme.shtml]. During the measurement period (1998-2007), the TRMM platform experienced a boost (Aug 24th, 2001) to extend the platform's lifetime. This changed the horizontal resolution at the Earth's surface from 4.3 to ~5 km. Our bilinear interpolation scheme re-projects the measurements from its orbital coordinates to an equally-spaced grid on the Earth surface (latitude/longitude grid). TRMM 2B31 data is a combined rainfall profile product from the Precipitation Radar (PR) and TRMM Microwave Imager (TMI). The TMI is a nine-channel passive microwave radiometer, which builds on the heritage of the Special Sensor Microwave/Imager (SSM/I) instrument [*Bookhagen et al.*, 2005a; *Hollinger*, 1990]. The Precipitation Radar (PR), the first of its kind in space, is an

electronically scanning radar operating at 13.8 GHz that measures the 3-D rainfall distribution over both land and ocean. The combined 2B31 algorithm uses the low-frequency channels of TMI to find the total path attenuation. This attenuation is used to constrain the radar equation to estimate the surface rain rate in mm/hr. We use root-mean square uncertainties of the surface-rainfall rate of each measurement to estimate the errors associated with each grid cell.

The TRMM algorithms that have been used for deriving rainfall amounts are interpreted to primarily represent rainfall amounts and do not include snowfall amounts. Remote sensing of snowfall is a difficult process, as snowflakes (or frozen precipitation) have different sizes, shapes, and densities resulting in complex radar echoes. In contrast, rain and raindrops consist of water, which has a known and fixed dielectric constant and thus is argued to interact with the radar wave in a predictable way. The sensors onboard the TRMM platform have been designed to sense tropical rainfall [*Kummerow et al.*, 1998]. However, on some of the higher peaks in the Karakoram (northern Pakistan) the TRMM algorithm predicts 4 m/yr rainfall at ~6 km elevation – a clearly unrealistic amount. Similarly, some of the high summits with persistent snow cover in the central Himalaya are associated with remotely-sensed rainfall amounts that are too high. We attribute this overestimation to potential scattering effects of snowfields. Although it is important to be aware of these discrepancies, the areas of the over-predicted rainfall amounts are only on the orders of several pixels and thus very small (< 100 km^2). They can safely be ignored on the spatial scales of catchments (3 to 250 $x10^3$ km^2) or entire mountain ranges on which we focus in this study.

We processed these data for 10 consecutive years from 1998 to 2007 with a total of 57,718 orbits (~16 each day). Because the orbital path of the TRMM satellite results in its own platform coordinate system, we bilinearly interpolated every orbit onto an equally-spaced 5 x 5 km^2 grid with a latitude/longitude reference frame on the Earth surface. The number of measurements (or observations) of the TRMM 2B31 data product depends on the number of overpassing orbits. This number, in turn, depends on the latitude: higher latitudes are observed more often, because the satellite's orbital path crosses them during the ascending and descending flights. In general, latitudes at ~35°N

have twice as many TRMM observations as the Himalayan foreland at ~28°N. In order to avoid overestimation of rainfall at higher latitudes, we explicitly correct for the time-dependent number of measurements as a function of latitude.

We have explicitly calculated the root mean square error for each measurement to account for satellite-derived uncertainties (Figure DR1). The combined (PR and TMI) product estimates errors by comparing predicted and measured brightness temperatures: large standard deviations imply that the measurements are too inconsistent with the physical model even after allowing for imperfections in the models and noise in the measurements. In contrast, small standard deviation indicate that the models can indeed explain the measurements if the parameters are given the values specific by the conditional means. Overall and throughout the Himalaya, our root mean square errors fit the physical model within 10% error (Figure DR1).

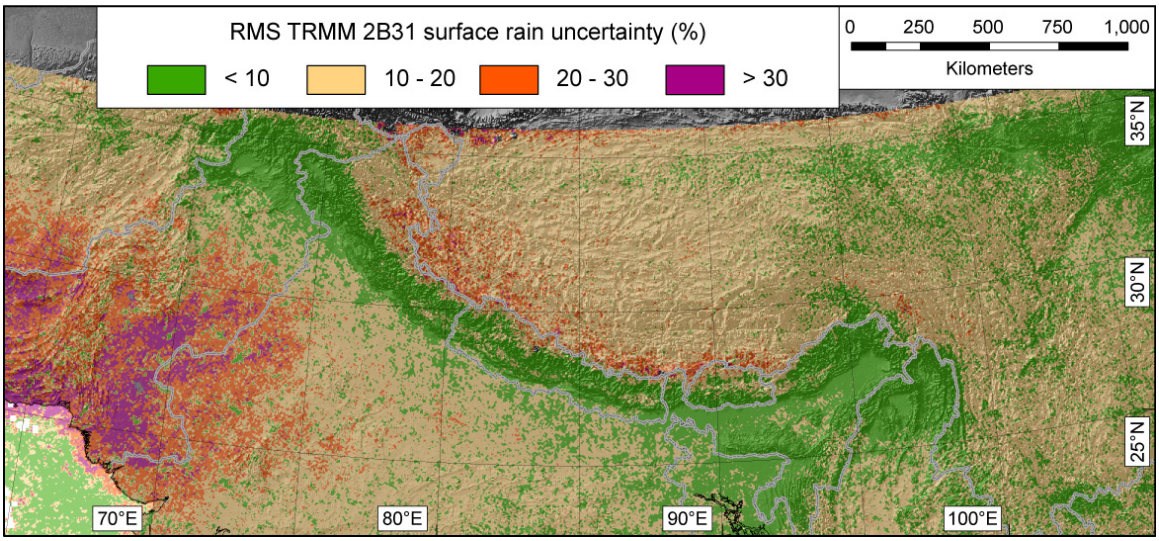

Figure DR1: Root-Mean-Square Errors of the surface rainfall (TRMM product 2B31) used in this study. We rely on satellite-retrieval errors (see text) and show the errors in percent compared to the absolute surface-rainfall amounts. Errors in our study area (Himalaya) are generally <10%, but are significantly larger in regions with lower rainfall amounts.

After scaling the data, the rainfall amounts were calibrated with daily, ground-based rainfall measurement from the mountainous areas of central Nepal and Bhutan (n = 19), and from the Indian subcontinent (n = 1722, see Figure 1 for location and Figure 2 to Figure 3 and Figure DR2 for calibrations) [*Barros et al.*, 2000; *Bookhagen and Burbank*,

2006; *GDCNV1*, 2002]. Generally, the data reveal robust and consistent results, even though the stations span >10° in latitudinal, >30° in longitudinal direction, and an elevation range from sea level to 4.5 km asl elevation (Figure DR2). Most of the heavy rainfall occurs below 4 km [*Barros et al.*, 2000; *Bookhagen and Burbank*, 2006; *Parthasarathy et al.*, 1992] and almost none above 6000 m [*Harper and Humphrey*, 2003]. We fitted the data using a robust least-squares method in which we minimize the summed square of the residuals and downweight outliers using bisquare weights. We have weighted the TRMM surface-rainfall rate with the root mean square estimates of the path attenuation fit. In order to derive a monthly rainfall dataset, we have calibrated mean monthly data averaged over the past 10 years using the same rain-gauge stations. We have removed unrealistically high rainfall intensities during orbit processing [*Iguchi et al.*, 2000; *Kozu et al.*, 2001]. Our calibration efforts and parameters match those from a similar study in the Andes of South America [*Bookhagen and Strecker*, 2008]. In general, the remotely-sensed rainfall data correlate very well with the ground-control stations: even high annual-rainfall amounts above 5 m/yr are accurately depicted (Figure 2 and Figure DR2). This corroborates our earlier findings from the Himalaya indicating that, despite non-continuous TRMM-rainfall data series, relative values represent a valid rainfall distribution [*Bookhagen and Burbank*, 2006].

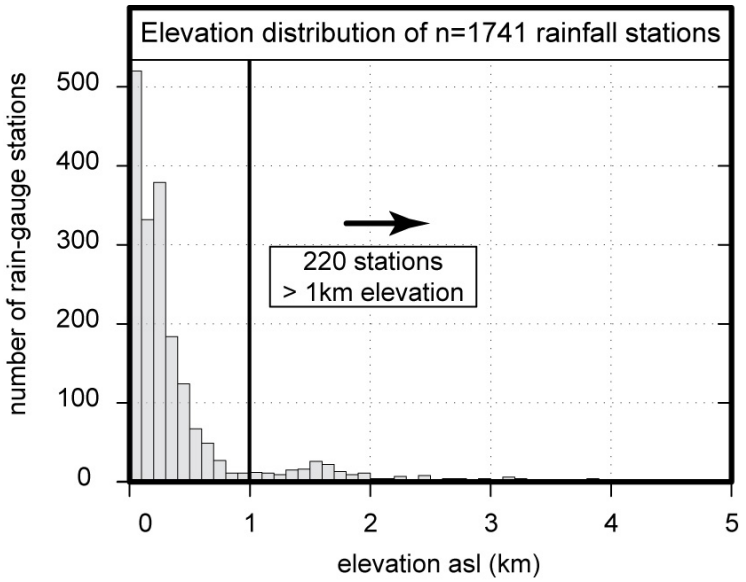

Figure DR2: Elevation histogram of rainfall stations (n=1741) used for calibration (see Figure 1B) for locations. The majority of the stations are from elevations below 1km, but there are more than 220 stations above 1km and more than a dozen stations above 3 km elevation.

Whereas the TRMM satellite captures most of the Himalaya, its orbital path does not include regions north of 36°N latitude. Thus, the northern parts of the Indus catchment are not covered by the high-resolution data. We, therefore, substituted these regions with the combined rainfall instrument calibration algorithm following 3B42, Version 6 [e.g., *Huffman et al.*, 2007; *Kummerow et al.*, 2000]. This algorithm uses an optimal combination of 2B31, 2A12, SSM/I (Special Sensor Microwave/Imager), AMSR (Advanced Microwave Scanning Radiometer), and AMSU (Advanced Microwave Sounding Unit) precipitation estimates. The output is gridded rainfall for 0.25x0.25 degree grid boxes (~30x30 km) on a 3-hour temporal resolution in a global belt extending from 50°S to 50°N. Although these data have a significantly lower spatial resolution, they provide rainfall estimates for the same time frame as the high-resolution TRMM product 2B31. The substituted part represents ~20% (~43 x 10^3 km^2) of the Indus catchment that has a total Himalayan drainage area of approximately 205 x 10^3 km^2. Because the substituted region lies in the high-elevation terrain with low annual rainfall amounts, use of a spatially lower-resolution dataset appears justified. In addition to patching the 2B31 dataset, we have created a mean-monthly time series of the 3B42 data.

We used both the high- (2B31) and low-spatial resolution (3B42) rainfall datasets to calculate the accumulated flow using the 90-m flow routing grid derived from the patched topographic data. We have routed the flow for every month, as well as an annual amount.

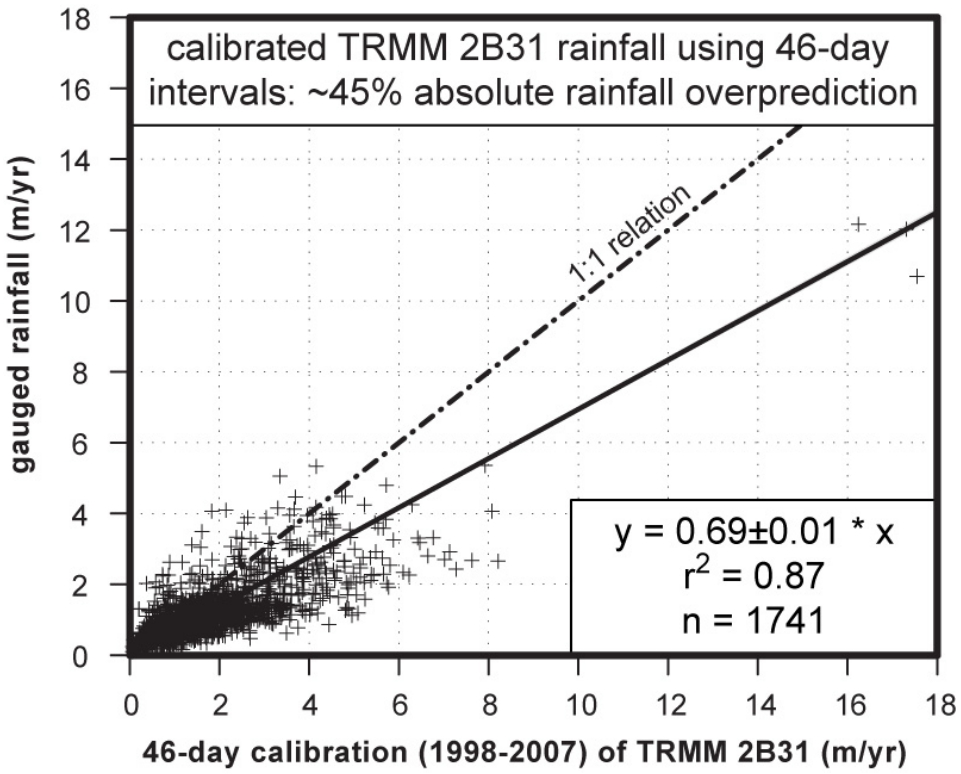

Figure DR3: Comparison of 46-day TRMM calibration (see text) with gauged rainfall (see Figure 1B for station locations). In this calibration routine, the year is divided into eight 46-day intervals – the period the TRMM satellites revisits a given location at the same time of day. Within this period, all measurements from different times of the day are averaged and multiplied by the length of the period. The relation with gauge rainfall is robust (r^2 = 0.87), but the 46-day calibration overpredicts rainfall by approximately 45%.

3. TRMM Lightning Image Sensor (LIS)

The Lightning Imaging Sensor (LIS) onboard the TRMM satellite consists of a staring imager, which is optimized to locate and detect lightning with storm-scale resolution (4 to 7 km) over a large region (~600 x 600 km) using a 128 x 128 charge coupled device (CCD) array [*Christian* et al., 1999]. We processed all available non-gridded, daily data between 1998 and 2006 (http://thunder.msfc.nasa.gov/data). The TRMM satellite travels a distance of 7 kilometers every second as it orbits the Earth, thus allowing the LIS to observe a point on the Earth or a cloud for almost 90 seconds as it passes overhead. Despite the brief duration of an observation, it is long enough to estimate the flashing rate of most storms. The LIS sensor records the time of occurrence, measures the radiant energy, and determines the location of lightning events within its field-of-view.

4. Snow-cover area, surface temperature, and solar radiation

We have used the MOD10C2 product, which is part of the MODIS snow products [*Hall et al.*, 2002; *Hall and Casey*, 2003]. The automated MODIS snow-mapping algorithm uses at-satellite reflectance in MODIS bands 4 (0.545-0.565 mm) and 6 (1.628-1.652 mm) to calculate the normalized difference snow index (NDSI) [*Hall et al.*, 2002]. A pixel in a non-densely forested region will be mapped as snow if the NDSI is ≥0.4 and reflectance in MODIS band 2 (0.841 – 0.876 mm) is >11%. However, if the MODIS band 4 reflectances is <10%, the pixel will not be mapped as snow even if the other criteria are met. There are some difficulties accurately identifying dense snow cover in vegetated areas [*Hall et al.*, 2002], but vegetation cover in the higher-elevated Himalaya, where most of the snow falls, is negligible.

In order to estimate land surface temperature, we have used the MODIS Land Surface Temperature (LST) product MOD11C, which has similar spatial and temporal characteristics as the MOD10C2 product [*Wan et al.*, 2004]. A variety of LST methods have been used and published – the MOD11 product relies on a split-window method that requires known surface emissivities to make correction for the atmospheric and surface emissivity effects based on the differential atmospheric absorption in the 10-13 mm split window [*Wan and Dozier*, 1996; *Wan et al.*, 2002]. This product retrieves surface spectral emissivities and temperatures from a pair of daytime and nighttime MODIS data, therefore generating a minimum and maximum temperature range. We have used an optimized and refined MODIS surface temperature product that estimates temperatures with a root mean square difference of less than 0.7°K [*Wan*, 2008]. These data are then used to calculate the days with a mean temperature above freezing.

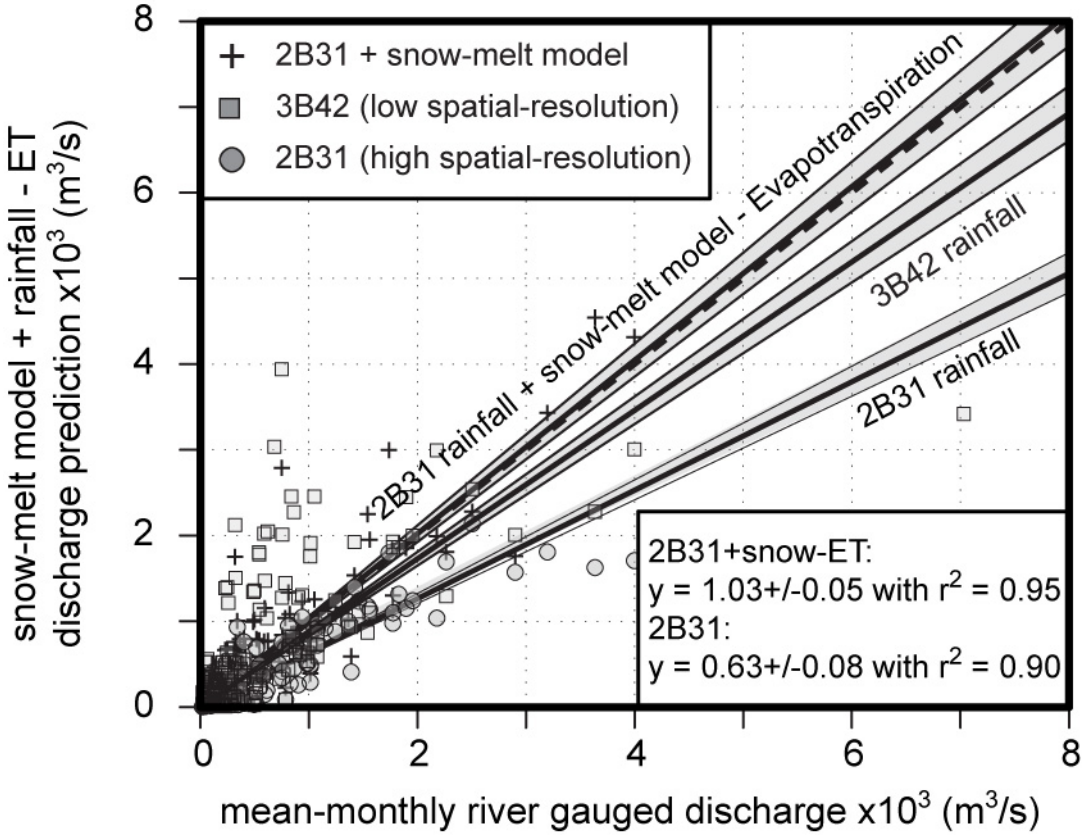

Figure DR4: Validation results of discharges derived from rainfall (2B31 and 3B42, snowmelt model and evapotranspiration. This figure is similar to Figure 4, but it includes results from the 3B42 climatology. We have used 13 stations (n = 12x13 = 156) that recorded daily discharge amounts during out modeling period (2000 to 2007) through the Himalaya. The bold dashed line indicates a 1:1 relation. The runoff from the TRMM3B42 rainfall is close to the measured discharge amounts and significantly higher than the TRMM2B31 rainfall. This is explained by the generally higher rainfall amounts over a larger area of the 3B42 dataset that result in higher discharge amounts, but overestimate grid-cell rainfall.

5. Evapotranspiration

The evapotranspiration (ET) amounts were derived from MODIS product MOD16 as described in *Cleugh et al.* [2007], *Mu et al.* [2007] and *Sun et al.* [2007]. This algorithm is based on the Penman-Monteith method and considers both the surface energy partitioning process and environmental constraints on ET [*Monteith*, 1964; *Cleugh et al.*, 2007]. The improved algorithm developed by *Mu et al.* [2007] was evaluated with 19 AmeriFlux eddy covariance flux towers and shows a robust ($r^2 = 0.76$) correlation with the field data.

In this study, the daily data were summed up per month and then averaged over a 7-year period to obtain mean monthly values. Similarly, the annual amounts were derived for each year before an average was calculated (Figure DR4).

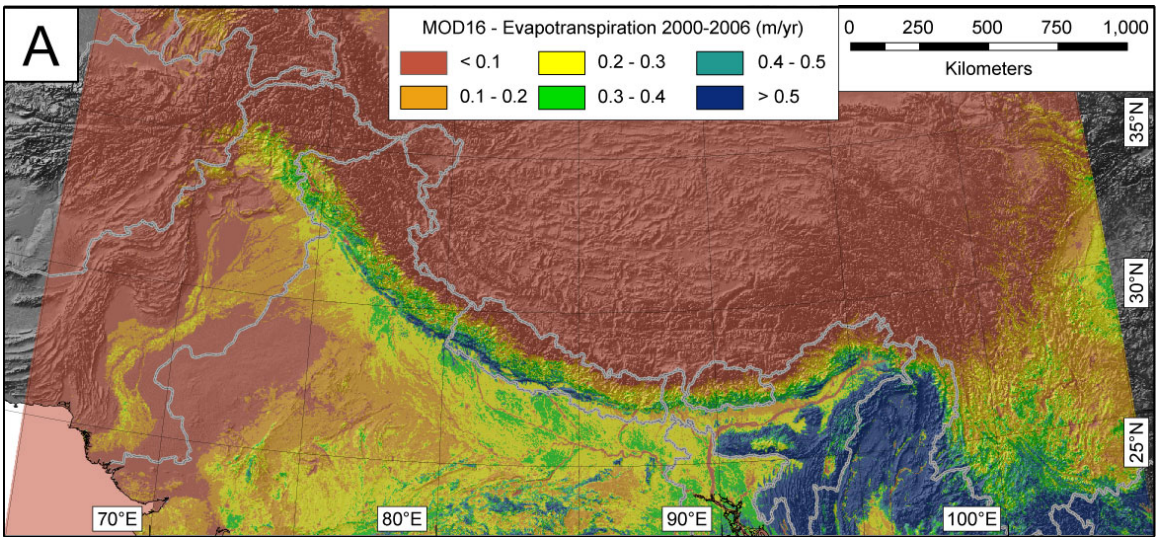

Figure DR5: Mean annual evapotranspiration (2000-2006) derived from the MODIS product MOD16 [Mu et al., 2007, Cleugh et al., 2007]. Note the high evapotranspiration amounts in the Himalayan foothills, the Ganges foreland, and the densely vegetated areas southeast of the Himalaya in the vicinity of the Shillong Plateau.

Results and Discussion

Based on our snowmelt model and the rainfall data, we calculated the fractional contribution made by snowmelt to the total discharge at any point in the catchment (see Figure 14). The map-based compilation reveals the importance of snowmelt throughout the year in the northwestern and northeastern Himalaya and at high elevations within the main Himalayan range (Figure DR6).

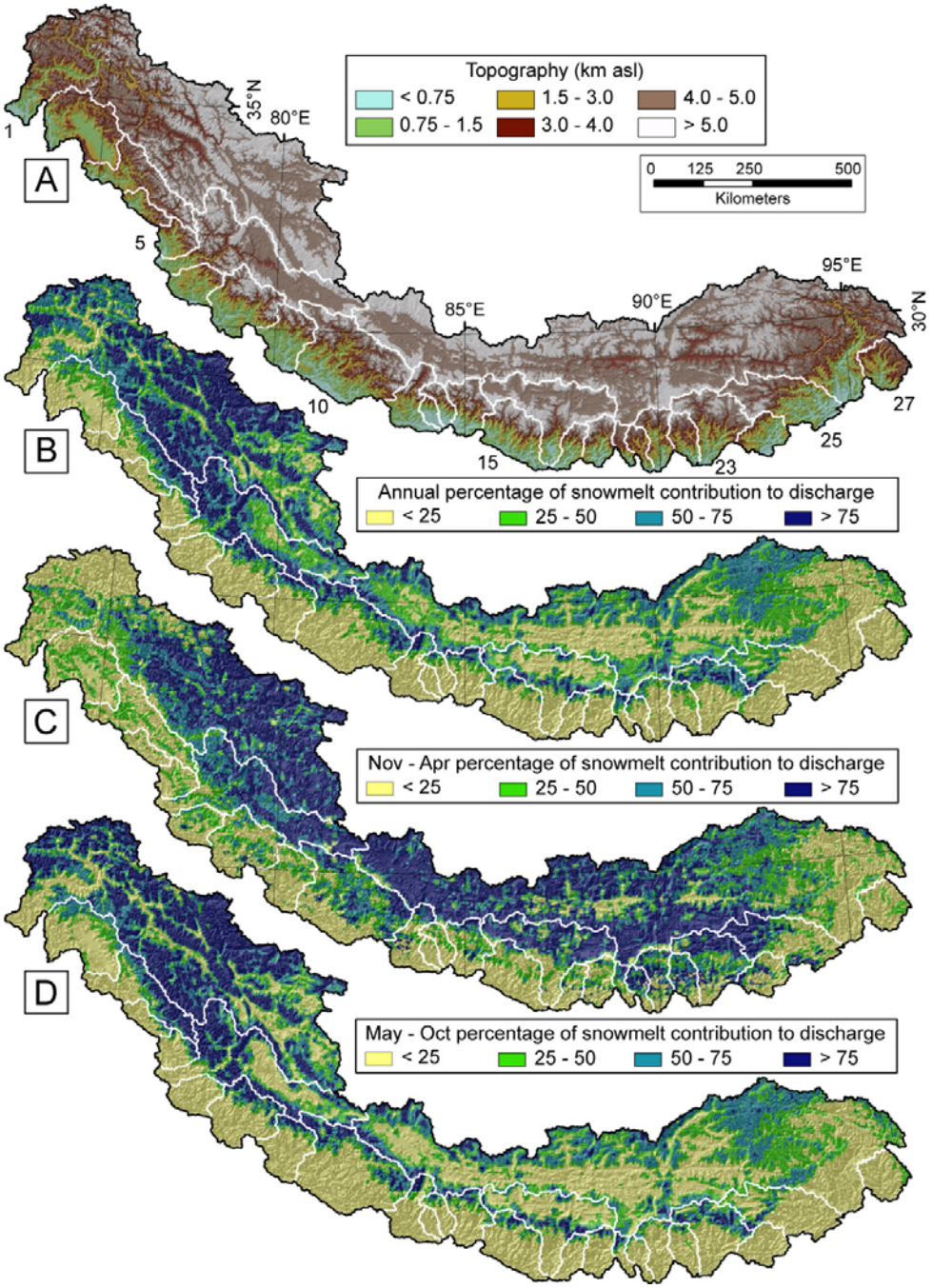

Figure DR 6: Overview and comparison of topography (A), annual (B) and seasonal (C-D) spatiotemporal discharge distribution derived from snowmelt. Note the high annual percentages (B) derived from snowmelt in the western catchments as well as in the high elevations along the Himalaya. The frontal areas are dominated by rainfall and thus have very low snowmelt contribution. During the winter (C), the southern parts of the Tibetan Plateau as well as high elevations area in all catchments contribute large amounts to river discharge. In the pre- and early-monsoon season (May to June), snowmelt from all catchments contributes significantly to river discharges (see also Figure 14 and 15).

In order to assess the quality of the snowmelt model and remotely sensed rainfall estimates, we compared our data to the gauged discharge from the Sutlej, Indus, and Titsa Rivers. Within the drier parts of the Sutlej catchment (<$3x10^{10}$ m^2), a linear log-log relationship exists of runoff versus area, irrespective of season (Figure DR7). Much higher rainfall south of the Himalayan crest (where catchment area exceeds $3x10^{10}$ m^2) drives abrupt increases in discharge and departure from the linear area-discharge relationship that exists upstream.

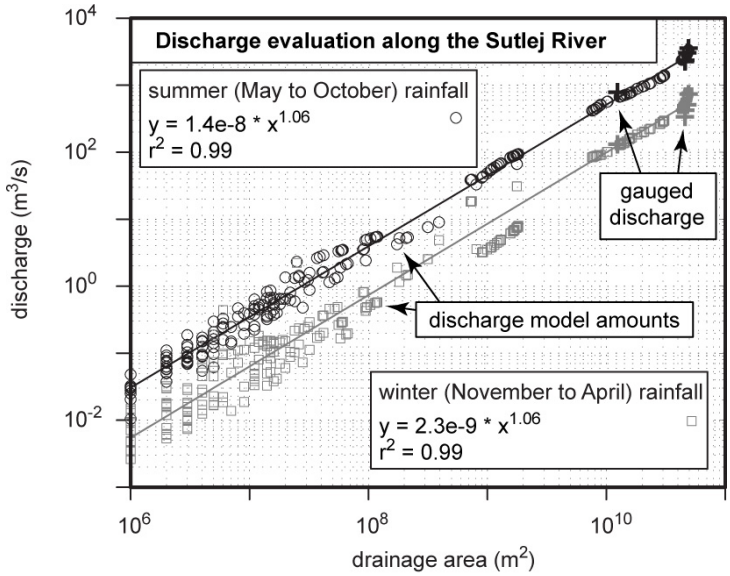

Figure DR7: Drainage area - discharge relation for the Sutlej River. Black circles show discharge during the summer, gray squares indicate winter discharge. Bold crosses are gauged discharge amounts. For both seasons, there is a robust power-law relation (r^2 = 0.99) between drainage area and discharge for most of the catchment. At drainage areas above $3x10^{10}$ m^2, discharge rapidly increases due to the influence of the monsoon.

Next, we analyze the relative rainfall and snowmelt contribution for the Sutlej River draining the southwestern Tibetan Plateau. During the summer time, discharge on the Tibetan Plateau side is dominated by rainfall contribution (~60%) and to a lesser degree by snowmelt contribution. This relation, however, changes downstream, when snowmelt from high-elevation ranges at the orographic barrier contributes more water to discharge. Only in the very downstream section near the southern end of the Himalaya, rainfall contribution becomes more important and reaches values above 50%.

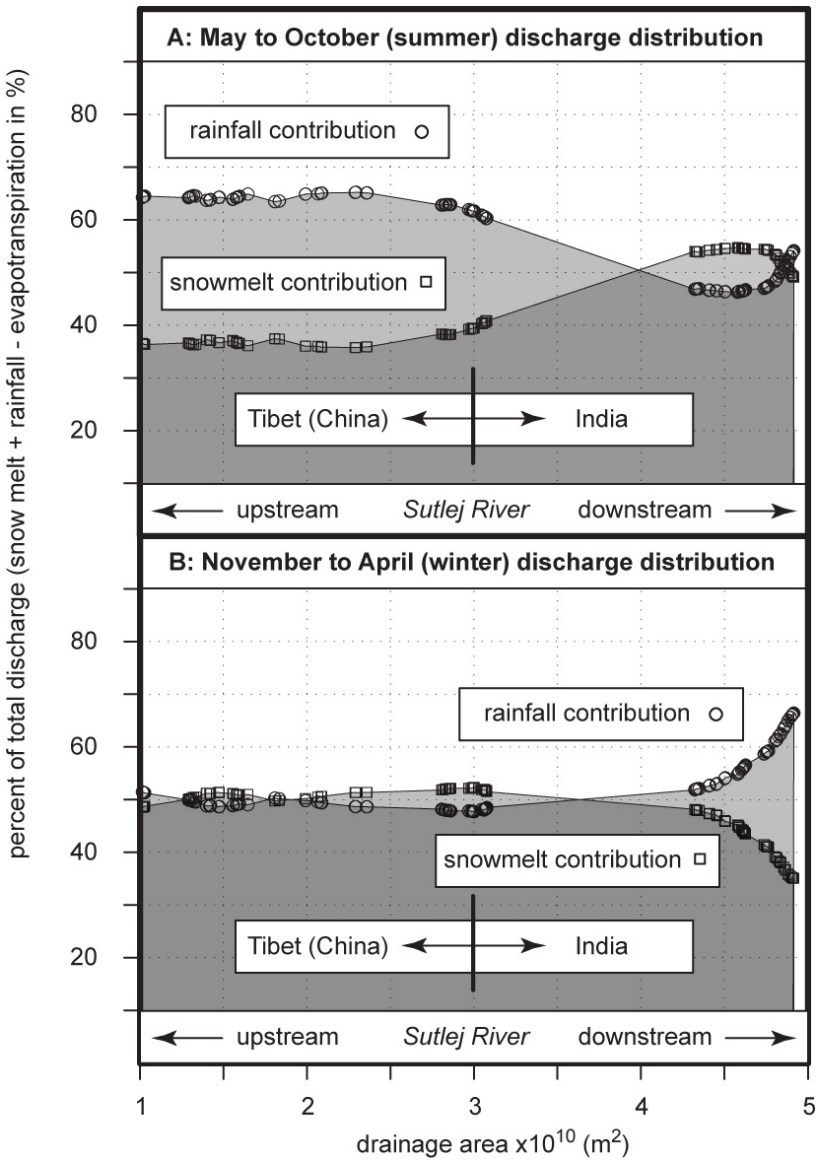

Figure DR8: Seasonal contribution of rainfall and snowmelt to total discharge for the Sutlej River. A shows summer and B winter season and focuses on drainage areas >10,000 km^2, encompassing the border region between China and India (see Figure 1 and DR1). During summer, rainfall dominates discharge amounts, except in the region of the orographic barrier (near 4.5 x 10^{10} m^2 in this figure), where high snow cover leads to a significant snowmelt contribution. During winter, discharge is dominated by rainfall only in the downstream, lower elevation areas. Note the large gaps between the points are due to drainage area increases when a tributary joins the Sutlej River.

References

Barros, A. P., and D. P. Lettenmaier (1994), Dynamic Modeling of Orographically Induced Precipitation, *Rev. Geophys.*, *32*(3), 265-284.

Bergeron, T. (1960), Operation and results of "Project Pluvius", in *Physics of Precipitation, Geophys. Monogr. Ser.*, edited by H. Weickmann, pp. 152-157, AGU, Washington, D.C.

Cleugh, H. A., et al. (2007), Regional evaporation estimates from flux tower and MODIS satellite data, *Remote Sensing of Environment*, *106*(3), 285-304.

Monteith, J. L. (1964), Evaporation and environment. The state and movement of water in living organisms, *Symposium of the society of experimental biology*, *Vol. 19*, 205-234, Cambridge: Cambridge University Press.

Mu, Q., et al. (2007), Development of a global evapotranspiration algorithm based on MODIS and global meteorology data, *Remote Sensing of Environment*, *111*(4), 519-536.

Roe, G. H. (2005), Orographic precipitation, *Annual Review of Earth and Planetary Sciences*, *33*, 645-671.

Smith, R. B. (1979), The influence of mountains on the atmosphere, *Advances in Geophysics*, *21*, 87-233.

Sun, Z. G., et al. (2007), Evaluation of MOD16 algorithm using MODIS and ground observational data in winter wheat field in North China Plain, *Hydrological Processes*, *21*(9), 1196-1206.